ACS APPLIED MATERIALS & INTERFACES

Research Article

www.acsami.org

Enhancement of the Visible-Light Photocatalytic Activity of In_2O_3–TiO_2 Nanofiber Heteroarchitectures

Jingbo Mu,[†] Bin Chen,*[,†] Mingyi Zhang,[‡] Zengcai Guo,[†] Peng Zhang,[‡] Zhenyi Zhang,[‡] Yangyang Sun,[‡] Changlu Shao,*[,‡] and Yichun Liu[‡]

[†]Department of Chemistry and [‡]Center for Advanced Optoelectronic Functional Materials Research, and Key Laboratory of UV Light-Emitting Materials and Technology of Ministry of Education, Northeast Normal University, 5268 Renmin Street, Changchun 130024, People' s Republic of China

ABSTRACT: One-dimensional In_2O_3–TiO_2 heteroarchitectures with high visible-light photocatalytic activity have been successfully obtained by a simple combination of electrospinning technique and solvothermal process. The as-obtained products were characterized by field emission scanning electron microscopy (FE-SEM), energy-dispersive X-ray (EDX) spectroscopy, transmission electron microscopy (TEM), X-ray diffraction (XRD), X-ray photoelectron spectroscopy (XPS), and UV–vis spectra. The results revealed that the secondary In_2O_3 nanostructures were successfully grown on the primary TiO_2 nanofibers substrates. Compared with the pure TiO_2 nanofibers, the obtained In_2O_3–TiO_2 heteroarchitectures showed enhancement of the visible-light photocatalytic activity to degrade rhodamine B (RB) because of the formation of heteroarchitectures, which might improve the separation of photogenerated electrons and holes derived from the coupling effect of TiO_2 and In_2O_3 heteroarchitectures. Moreover, the In_2O_3–TiO_2 heteroarchitectures could be easily recycled without the decrease in the photocatalytic activity because of their one-dimensional nanostructural property.

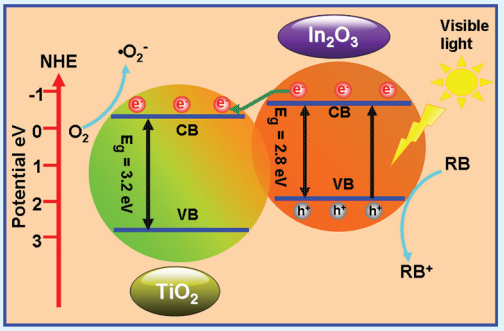

KEYWORDS: *In_2O_3, TiO_2, heteroarchitectures, photocatalysis, degradation*

1. INTRODUCTION

With the development of industry and economy of human society, environmental problems are becoming more and more serious. Since Fujishima and Honda reported the evolution of oxygen and hydrogen from a TiO_2 electrode under the irradiation of light in 1972,[1] photocatalysis was regarded as one of the most effective and economical ways to solve the environmental problems. Thus, in recent years, many kinds of semiconductor metal oxide photocatalyst, such as Bi_2O_3, Fe_2O_3, ZnO, TiO_2 and so forth, have been developed for creating a comfortable environment for human beings.[2−7] In particular, titanium dioxide (TiO_2) has been widely studied as a semiconductor photocatalyst for potential application in air purification and photocatalytic degradation of organic pollutants owing to its excellent (photo) chemical stability, low cost and nontoxicity.[8−13] However, the application of TiO_2 is limited by its large band gap energy (3.2 eV for anatase), which limits its photoresponse only to the ultraviolet (UV) region. Unfortunately, only a small ultraviolet (UV) fraction (<4%) of the total solar spectrum reaching the surface of the earth.[14] Therefore, how to make TiO_2 responsive to visible light in photocatalysis becomes an important subject for developing the TiO_2-based photocatalysts. In the past decade, many attempts have been made to extend the photoresponse of the TiO_2 to visible region.[15−27] Among these attempts, TiO_2 doping with transitionmetals ions or nonmetal elements, such as V, Co, Fe, C, N, S, or I, has been a common approach for improving the photocatalytic performance of the catalyst.[28,29] Although the above modifications could partly improve the photocatalytic activity of TiO_2, some key problems remain unresolved, for example, doped materials suffer from thermal instability, photo corrosion, lattice distortion, and an increase in the carrier-recombination probability.[30] One of the promising strategies to overcome this drawback is to couple TiO_2 with other narrow band gap semiconductors serving as the sensitizer to absorb visible light.

In_2O_3, an indirect band semiconductor with a direct band gap of 3.6 eV and an indirect band gap of 2.8 eV,[31] had proved to be an efficient sensitizer to extend the absorption spectra of oxide semiconductor photocatalysts from the UV region into the visible region.[32−34] Moreover, the coupling of two different semiconductors could transfer electrons from an excited small band gap semiconductor into another attached one in the case of proper conduction band potentials. This favors the separation of photoinduced electrons and holes and thus improved the photocatalytic efficiency of semiconductor heterostructure dramatically. Considering the band gap of In_2O_3 (E_g = 2.8 eV) is lower than that of TiO_2 (E_g = 3.0 eV for rutile, E_g = 3.2 eV for anatase), but the conduction band (CB) of In_2O_3 (E_{CB} for In_2O_3 = −0.63 V versus NHE) is higher than

Received: October 29, 2011
Accepted: December 12, 2011
Published: December 12, 2011

that of TiO_2 (E_{CB} for TiO_2 = −0.4 V versus NHE), an efficient heterostructure could be formed for the separation of photogenerated charge carriers when coupling them together. Recently, a rich variety of In_2O_3−TiO_2 photocatalysts have been prepared, including nanoparticles, films, and so on.[35−40] Among these materials, the In_2O_3−TiO_2 nanopowders exhibit a high photocatalytic activity because of their high surface area. However, it is often limited, because the suspended particulate catalysts are easily lost in the process of photocatalytic reaction and separation, which may repollute the treated water again. Meanwhile, the In_2O_3−TiO_2 films can be fixed and reclaimed easily, but their photocatalytic activity is decreased because of their low surface area. Compared with the corresponding nanoparticles and thin films of In_2O_3−TiO_2, the one-dimensional nanomaterials of the In_2O_3−TiO_2 possessed high photocatalytic activity and favorable recycling characteristics due to its high surface area and one-dimensional properties, which might be deemed as potential good candidates for practical application. However, to the best of knowledge, there has been no report on the preparation and photocatalytic properties of these kinds of materials.

Motivated by the above concerns, we fabricate one-dimensional In_2O_3−TiO_2 heteroarchitectures photocatalysts based on TiO_2 nanofibers by combining the electrospinning technique with the solvothermal method. And the photocatalytic activity of these heteroarchitectures photocatalysts in the visible-light region are investigated by measuring the degradation of dye RB as a test substance. The experimental results showed that the as-obtained In_2O_3−TiO_2 heteroarchitectures exhibited excellent visible light photocatalytic activity. Moreover, due to the large length to diameter ratio of TiO_2 nanofibers, the In_2O_3−TiO_2 heteroarchitectures could be reclaimed easily by sedimentation without a decrease of the photocatalytic activity. Finally, the mechanisms of visible photocatalysis in In_2O_3−TiO_2 heteroarchitectures were proposed.

2. MATERIALS AND METHODS

2.1. Preparation of TiO_2 Nanofibers. First, 2 g of poly (vinylpyrrolidone) powder (PVP, M_w = 1 300 000) was added to a mixture of 9 mL of absolute ethanol and 5 mL of acetic acid in a capped bottle. The obtained solution was stirred for 1 h to generate a homogeneous solution. Then, 2.0 g $Ti(OC_4H_9)_4$ was added to the solution, and the mixture was continuously stirred for another 1 h to make precursor solution. Three milliliters of the precursor solution was placed in a 5 mL syringe equipped with a blunt metal needle of 0.8 mm outer diameter and 0.6 mm inner diameter. A stainless steel plate covered with a sheet of aluminum foil was employed as the collector. The distance between the needle tip and collector was 15 cm, and the voltage was set at 9 kV. The as-collected nanofibers were calcined at 550 °C for 2 h to form anatase TiO_2 nanofibers.

2.2. Fabrication of In_2O_3−TiO_2 Heteroarchitectures. In a typical experiment, 0.3 mmol $In(NO_3)_3{\cdot}5H_2O$, 1 g $CO(NH_2)_2$ were dissolved in the mixture of 13 mL of diethylene glycol (DEG) and 2 mL of H_2O under magnetic stirring. The resulting solution and the obtianed TO_2 (15 mg) was transferred into a 20 mL Teflon-lined stainless autoclave, sealed and maintained at 200 °C for 24 h, and then cooled down to room temperature. The as-fabricated products were collected out, washed several times with ethanol and deionized water, respectively, then dried at 60 °C for 12 h. Thus, the In_2O_3−TiO_2 heteroarchitectures were fabricated, which was denoted as IT1. By this method, the samples IT2 was prepared at the additive amount of $In(NO_3)_3{\cdot}5H_2O$ was 0.6 mmol. In addition, for simplicity, pure TiO_2 nanofibers were denoted as IT0. For contrast, the pure In_2O_3 was obtained in the absence of TiO_2 during the process of prepartion of the In_2O_3−TiO_2 heteroarchitectures and ready for further test.

2.3. Characterization. The scanning electron microscopy (SEM, XL-30 ESEM FEG, Micro FEI Philips) and transmission electron microscopy (TEM; high resolution TEM [HRTEM], JEM-3010) were used to characterize the morphologies of the products. Energy dispersive X-ray (EDX) spectroscopy being attached to scanning electron microscopy (SEM) was used to analyze the composition of samples. X-ray diffraction (XRD) measurement was carried out using a D/max 2500 XRD spectrometer (Rigaku) with Cu Ka line of 0.1541 nm. X-ray photoelectron spectroscopy (XPS) was performed on a VG ESCALAB LKII instrument with Mg KR-ADES ($h\nu$ = 1253.6 eV) source at a residual gas pressure of below 1×10^{-8} Pa. The UV−vis diffuse reflectance (DR) spectroscopy of the samples were recorded on a Cary 500 UV−vis−NIR spectrophotometer for wavelengths from 200 to 800 nm (the irradiation time was 40 s). The photoluminescence (PL) spectra of photocatalysts were detected with a Jobin Yvon HR800 micro-Raman spectrometer using a 325 nm line from a He−Cd laser. The specific surface areas of the samples were measured with a Micromeritics ASAP 2010 instrument and analyzed by the BET method.

2.4. Photocatalytic test. The photoreactor was designed with an internal xenon lamp (XHA 150W) equipped with a cutoff glass filter transmitting λ > 420 nm surrounded by a water-cooling quartz jacket to cool the lamp, where a 100 mL of the RB solution with an initial concentration of 10 mg L^{-1} in the presence of solid catalyst (0.05 g). The solution was stirred in the dark for 30 min to obtain a good dispersion and establish adsorption−desorption equilibrium between the organic molecules and the catalyst surface. Decreases in the concentrations of dyes were analyzed by a Cary 500 UV−vis−NIR spectrophotometer. At given intervals of illumination, the samples of the reaction solution were taken out and then centrifuged and filtered. Finally, the filtrates were analyzed.

3. RESULTS AND DISCUSSIONS

The morphology of the samples were observed by FESEM, which were shown in Figure 1. Figure a1 and a2 showed the

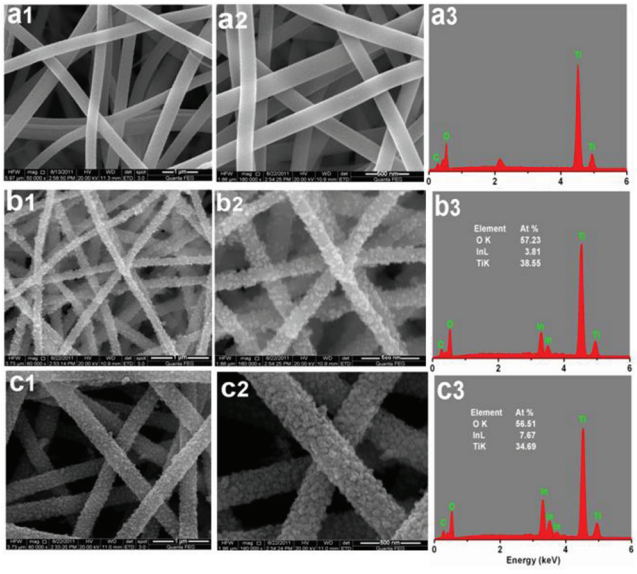

Figure 1. (a1, a2) SEM images of sample IT0 with different magnifications; (b1, b2) SEM images of sample IT1 with different magnifications; (c1, c2) SEM images of sample IT2 with different magnifications; (a3) EDX spectrum of sample IT0; (b3) EDX spectra of sample IT1 and IT2 (c3).

typical SEM images of the electrospun TiO_2 nanofibers before solvothermal treatment. From image a1, it could be observed

dx.doi.org/10.1021/am201499r | ACS Appl. Mater. Interfaces 2012, 4, 424−430

that the pure TiO_2 aligned in random orientation because of the bending instability associated with the spinning jet. Image a2 displays the corresponding SEM image with higher magnification. It was showed that these randomly oriented TiO_2 had a smooth and uniform surface without secondary nanostructures, and the diameter of the TiO_2 ranged from 120 to 250 nm. After solvothermal treatment, the as-fabricated sample remained as a nonwoven nanofibrous morphology, as shown in image b1. However, the surface of the TiO_2 was no longer smooth. Instead, the nanofibers were decorated with numerous secondary nanoparticles. Image b2 was the higher-magnification image of the sample IT1, it could be observed that the nanoparticles were uniformly distributed across the surface of each fiber, offering the high level exposure of the nanoparticles' surface. Images c1 and c2 revealed the different magnified image of sample IT2. It could be observed that the density of the nanoparticles was dramatically increased when the precursor molar ratio of reactants was increased. It was worth pointing out that the surface area of TiO_2 was advantageous for uniform growth and distribution of In_2O_3 nanoparticles on the surface of TiO_2. Images a3, b3, and c3 were the energy-dispersive X-ray (EDX) spectrum of the samples TiO_2, IT1 and IT2, respectively. It was indicated that C, O and Ti elements existed in pure electropun TiO_2, while C, O, Ti and In existed in the In_2O_3–TiO_2 heteroarchitectures (IT1 and IT2), respectively. C peaks in images a3, b3, and c3 were attributed to the FESEM platform used to support the nanofibers. The EDX analysis results showed that the atomic ratios of In to Ti were about 1/10 and 11/50 for IT1and IT2, respectively. Accordingly, the mass percentage of In_2O_3 in the In_2O_3–TiO_2 heteroarchitectures could be determined as 15 and 28% for IT1and IT2, respectively. The EDX spectra further confirmed that the In_2O_3–TiO_2 heteroarchitectures were successfully fabricated.

To obtain the microstructure of the In_2O_3–TiO_2 heteroarchitectures, the TEM images depicted in Figure 2 provided a

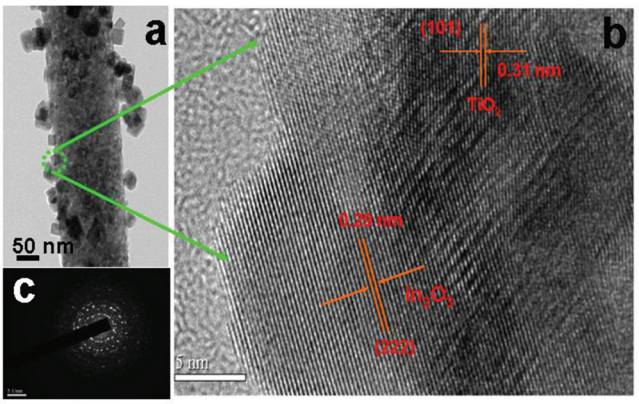

Figure 2. (a) TEM image of the sample IT1. (b) HRTEM image of the sample IT1. (c) SAED pattern of sample IT1.

clear observation of the as-synthesized IT1 sample. The low magnification TEM image of the In_2O_3–TiO_2 heteroarchitectures was displayed in Figure 2a. It could be seen that the ultrasonic process during the sample preparation for TEM measurements did not caused the In_2O_3 nanoparticles to fall off the TiO_2, it indicated that In_2O_3 nanoparticles had been successfully grown onto the surface of the TiO_2. Moreover, it could be observed that the diameter of TiO_2 was about 130 nm, which was in agreement with the SEM analysis above. And the In_2O_3 nanoparticles possessed the average size about 20–30 nm. Meanwhile, a high-resolution image of the In_2O_3–TiO_2 heteroarchitectures obtained from the area marked with a circularity in Figure 2a were shown in Figure 2b. The junction displayed two types of clear lattice fringes as shown in Figure 2b, one set of the fringes spacing was *ca.* 0.31, corresponding to the (101) plane of the anatase crystal structure of TiO_2. Another set of the clear fringes spacing measures ca. 0.29 nm, which corresponded to the (222) lattice spacing of the cubic phase of In_2O_3. In Figure 2c, the corresponding ringlike selected-area electron diffraction (SAED) pattern indicated the nanoparticles had a polycrystalline structure. These results confirmed that the heteroarchitectures were well-formed between TiO_2 nanoparticles and In_2O_3.

The X-ray diffraction (XRD) patterns of the as-obtained samples IT1, IT2 and pure TiO_2 were shown in Figure 3.

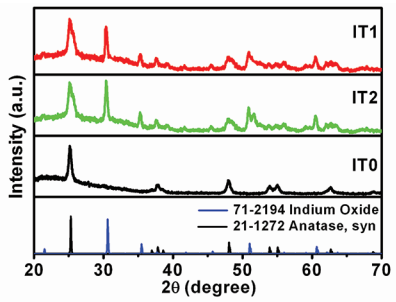

Figure 3. XRD patterns of In_2O_3–TiO_2 heteroarchitectures (IT1, IT2) and pure TiO_2 nanofibers (IT0).

The curve a in Figure 1 revealed that the crystal phase of TiO_2 nanofibers was anatase with the diffraction peaks at about 2θ = 25.5, 37.9, 48.2, 54.1, 55.0, and 62.8°, which could be perfectly indexed to the (101), (004), (200), (105), (211) and (204) crystal faces of anatase TiO_2 (PDF card 21–1272, JCPDS). After solvothermal treatment at 200 °C for 24 h, as shown in samples IT1 and IT2, additional diffraction peaks with 2θ values of 30.42, 35.28, 50.94, and 60.52° appeared, which could be perfectly indexed to the (222), (400), (440), and (622) crystal planes of the body-centered cubic (bcc) In_2O_3 crystalline phase with a lattice constant of a = 10.1 Å ((PDF card 71–2194, JCPDS). No characteristic peaks for impurity, such as In, $In(OH)_3$ or $InTiO_5$ were observed, suggesting that the composition of the above nanofibers was In_2O_3 and TiO_2. Moreover, the average grain sizes of the products was calculated by applying the Debye–Scherrer formula, $D = K\lambda/(\beta\cos\theta)$, where λ was the wavelength of the X-ray radiation (Cu Kα = 0.15406 nm), K was a constant taken as 0.89, β was the line width at half-maximum height, and θ was the diffracting angle. The average particle size had been calculated using the three different prominent planes of (222), (400), and (440) with mean values of 28.89 and 35.26 nm for IT1 and IT2, respectively. It was worthwhile to note that the diffraction peaks of In_2O_3 in IT1 and IT2 were sharp and intense, implying the high crystallinity of the In_2O_3 nanocubes in the In_2O_3–TiO_2 heteroarchitectures.

To confirm the chemical composition and purity of the prepared heteroarchitectures, the sample IT1 was further studied and compared with those of the pure TiO_2 nanofibers (IT0) by XPS analysis. The fully scanned spectra (Figure 4a) showed that elements In, Ti, O and C existed in In_2O_3–TiO_2

dx.doi.org/10.1021/am201499r | *ACS Appl. Mater. Interfaces* 2012, 4, 424–430

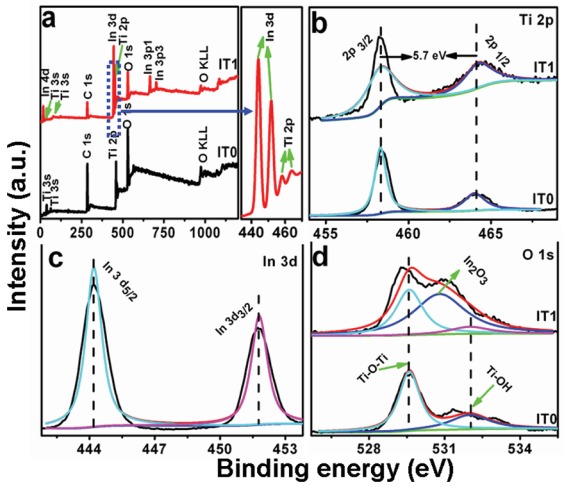

Figure 4. (a) XPS fully scanned spectra of the typical In_2O_3–TiO_2 heteroarchitectures (IT1) and pure TiO_2 nanofibers (IT0); (b) XPS spectra of Ti 2p for the typical In_2O_3–TiO_2 heteroarchitectures (IT1) and pure TiO_2 nanofibers (IT0); (c) XPS spectrum of In 3d for the In_2O_3–TiO_2 heteroarchitectures (IT1); (d) XPS spectra of O1s for In_2O_3–TiO_2 heteroarchitectures (IT1) and pure TiO_2 nanofibers (IT0).

heteroarchitectures, while, Ti, O and C elements existed in bare TiO_2 nanofibers, respectively. The C element could be ascribed to the adventitious carbon-based contaminant, and the binding energy for C 1s peak at 284.6 eV was used as the reference for calibration. The high-resolution XPS spectra with scanning over the area corresponding to the binding energies for the Ti 2p region around 460 eV were analyzed in Figure 4b. For the sample IT1, the peak located at 464.2 eV corresponds to the Ti $2p_{1/2}$ and another one located at 458.5 eV was assigned to Ti $2p_{3/2}$. The splitting between Ti $2p_{1/2}$ and Ti $2p_{3/2}$ was 5.7 eV, indicating a normal state of Ti^{4+} in the In_2O_3–TiO_2 heteroarchitectures. Besides, the peaks for Ti 2p in the sample IT1 showed no shift compared with that in pure TiO_2 nanofibers, confirming that the structure of TiO_2 remained intact after synthesis of In_2O_3–TiO_2 heteroarchitectures. Figure 4c revealed the high resolution XPS spectra for the In 3d, because of the spin–orbital splits, the In $3d_{5/2}$ and In $3d_{3/2}$ XPS peaks also had characteristic double peaks centered at binding energies of 444.2 and 451.8 eV, respectively. Compared with the reported In $3d_{5/2}$ signal of metallic indium, which appeared at 443.6 eV, the absence of this peak excluded the existence of metallic indium, and indicated that in the element indium in In_2O_3–TiO_2 heteroarchitectures existed in the oxide state only.[41] The O 1s XPS spectrum could be resolved using the XPS peak fitting program, version 4.1. Figure 4d presented the O 1s photoelectron peaks. For the pure TiO_2 nanofibers (IT0), there existed only two oxygen signals, at 529.6 and 532 eV, that were attributed to Ti–O–Ti (lattice O) and Ti–OH, respectively,[42] whereas for the In_2O_3–TiO_2 heteroarchitectures (IT1), obviously, a new oxygen signal at 530.7 eV appeared that could be indexed to oxygen anions from indium oxide.[43] All of these results gave the insight that the heteroarchitectures were composed of In_2O_3 and TiO_2. The relative quantitative analysis of each element was completed using the XPS peak area data of different elements and their respective elemental sensitivity factor according to the equation below

$$n(\mathrm{E1})/n(\mathrm{E2}) = [A(\mathrm{E1})/S(\mathrm{E1})]/[A(\mathrm{E2})/S(\mathrm{E2})] \quad (1)$$

where n was the number of the atom, Ei was the element i, A was the peak area, and S was the elemental sensitivity factor.[44] The sensitive factor S of In $3d_{5/2}$ and Ti 2p was 3.77, and 1.80, respectively. Here, the molar ratio of Ti to In was 19.8:2.1. The result showed that the value calculated was close to the EDX analyses.

The diffuse reflectance spectra for the synthesized In_2O_3–TiO_2 heteroarchitectures were presented in Figure 5.

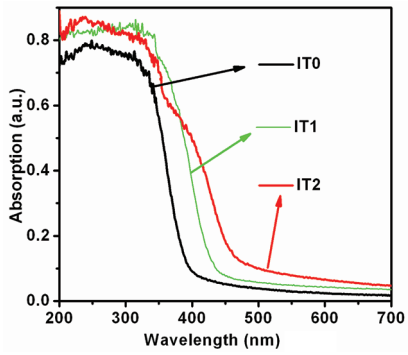

Figure 5. UV–vis spectra of different samples.

For comparison, the spectra of pure TiO_2 and In_2O_3 synthesized under identical conditions were also plotted. As could be seen from the curve of pure TiO_2 nanofibers, TiO_2 nanofibers showed a clear absorption edge at about 390 nm, and only exhibited the fundamental absorption in the UV region. For the heteroarchitectures, the curves of samples IT1 and IT2 exhibited the a mixed absorption property of both TiO_2 and In_2O_3. Moreover, the visible light absorbance was increased with the increase in density of the In_2O_3 grown on TiO_2 nanofibers.

To demonstrate the photoactivity of the as-obtained In_2O_3–TiO_2 heteroarchitectures for the degradation of organic pollutants, we had carried out the experiments of the photocatalytic degradation of rhodamine B (RB) as a test reaction. Furthermore, in the comparative experiments, the pure TiO_2 (IT0) In_2O_3 and the Degussa-P25 were used as a photocatalytic reference to understand the photocatalytic activity of the In_2O_3–TiO_2 heteroarchitectures. The change of absorption spectra of RB aqueous solution showed the change of its concentration. The initial concentration (C_0), the final concentration (C), and the degradation rate (D%) had a mathematical expression as follows

$$D\% = \frac{C_0 - C}{C_0} 100\% \quad (2)$$

As observed in Figure 6a, the control experiments were performed under different conditions: (1) in the presence of photocatalysts but in the dark and (2) with visible light irradiation but in the absence of the photocatalysts. These control experiments revealed that there was no appreciable degradation of RB over the In_2O_3–TiO_2 heteroarchitectures in the absence of visible light irradiation, indicating that the adsorption of RB on the In_2O_3–TiO_2 heteroarchitectures could be negligible. And, there was no appreciable degradation of RB after 4 h in the absence of photocatalysts. Figure 6b showed the degradation curves of RB on the Degussa-P25, In_2O_3, TiO_2 nanofibers, IT1 and IT2. It could be seen that the Degussa-P25 had no photocatalytic activity under the visible light, except

dx.doi.org/10.1021/am201499r | ACS Appl. Mater. Interfaces 2012, 4, 424–430

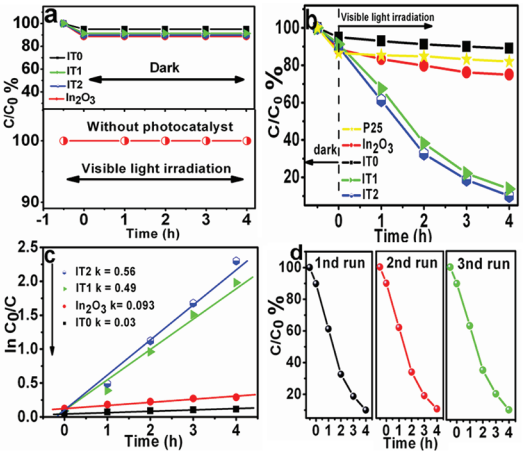

Figure 6. (a) Degradation profiles of RB in the presence of the photocatalysts but in the dark and with UV light irradiation but in the absence of the photocatalysts. (b) Degradation profiles of RB over the samples: IT0, IT1, IT2, Degussa-P25 and In_2O_3 (C_0 = 10 mg/L, catalyst 0.05 g). (c) Kinetic linear simulation curves of RB photocatalytic degradation with samples: IT0, IT1, IT2 and In_2O_3. (d) Photocatalytic activity of the In_2O_3–TiO_2 heteroarchitectures (IT2) for RB degradation with three times of cycling uses.

decent adsorption for RB, which could be attributed to the high specific surface area of the samples. Meanwhile, only 11% of RB molecular for TiO_2 and 25% for In_2O_3 were decomposed in 4 h. In comparison, after visible light irradiation for 4 h, the degradation efficiency of RB were about 86 and 90% for the IT1 and IT2, respectively. Obviously, the In_2O_3–TiO_2 heteroarchitectures showed much higher photocatalytic activities than that of TiO_2 and In_2O_3. So RB could be degraded efficiently when visible light was used as the light source in the presence of the In_2O_3–TiO_2 heteroarchitectures photocatalyst. We studied the BET of IT1 and IT2. The surface areas of IT1 and IT2 were 10.83 and 11.59 $m^2\ g^{-1}$, respectively. The larger BET surface area could facilitated more efficient contact of the In_2O_3–TiO_2 nanofibers heteroarchitectures with organic contaminants and thus improved its photocatalytic activity. As a result, the photocatalytic activity of IT2 and IT1 were different. The kinetic linear simulation curves of the photocatalytic degradation of RB over the above catalysts showed that the above degradation reactions followed a Langmuir–Hinshelwood apparent first-order kinetics model due to the low initial concentrations of the reactants. The explanation was described below[45]

$$r = dC/dt = kKC/(1 + KC) \quad (3)$$

where r was the degradation rate of the reactant (mg/(L min)), C was the concentration of the reactant (mg/L), t was the UV light irradiation time, k was the reaction rate constant (mg/(Lmin)), and K was the adsorption coefficient of the reactant (L/mg). When the initial concentration (C_0) was very low (C_0 = 10 mg/L for RB in the present experiment), eq 2 could be simplified to an apparent first-order model[46]

$$\ln C_0/C = kKt = k_{app}t \quad (4)$$

where k_{app} was the apparent first-order rate constant (min^{-1}). The determined k_{app} for different catalysts were summarized in Figure 6c. The photocatalytic reactivity order was IT2 > IT1 > In_2O_3 > IT0. Moreover, the stability of the In_2O_3–TiO_2 heteroarchitectures (IT2) was examined for degradation of RB during a three cycle experiment, which was very important for the In_2O_3–TiO_2 heteroarchitectures to apply in environmental technology. As shown in Figure 6d, the photocatalytic degradation of RB over the In_2O_3–TiO_2 heteroarchitectures under visible light irradiation was effective. More importantly, it was indicated that these heteroarchitectures nanofibers photocatalysts with high photocatalytic activity could be easily separated and recovered by sedimentation, and would greatly promote their practical application to eliminate the organic pollutants from wastewater.

On the basis of the above results, a proposed mechanism was being discussed to explain the enhancement of the photocatalytic properties of the In_2O_3–TiO_2 heteroarchitectures. The conduction band (CB) bottom and the valence band (VB) top of TiO_2 lie at −0.4 and 2.8 eV with respect to NHE,[47] and the CB bottom and VB top of In_2O_3 lie at −0.63 and 2.17 eV versus NHE.[32] As illustrated in Figure 7a, both the CB bottom

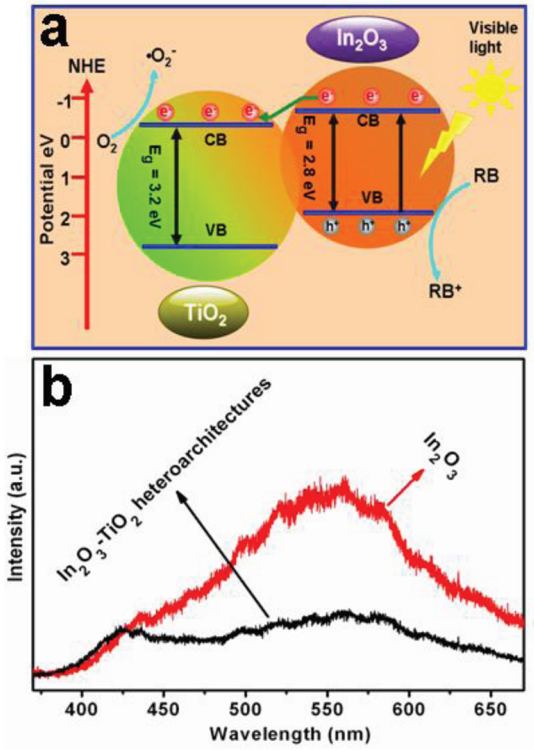

Figure 7. (a) Schematic diagram showing the energy band structure and electron–hole pair separation in the In_2O_3–TiO_2 heteroarchitectures. (b) PL emission spectra of In_2O_3 and In_2O_3–TiO_2 heteroarchitectures.

and the VB top of TiO_2 lay below the CB bottom and VB top of In_2O_3, respectively. When they were coupled together to form a heterostructure, the In_2O_3 could be excited under visible light irradiation and the generated electrons in the In_2O_3 were then migrated to the conduction band (CB) of TiO_2. Moreover, due to the high crystallinity of the In_2O_3, the resistance of electron transport was very low and reduced electron–hole recombination. Consequently, the efficient charge separation increased the lifetime of the charge carriers and enhanced the efficiency of the interfacial charge transferred to the adsorbed substrates, leading to higher activity of the In_2O_3–TiO_2 heteroarchitectures photocatalyst. Furthermore, the better separation of photogenerated electrons and holes in the In_2O_3–TiO_2 heteroarchitectures was confirmed by PL emission spectra of

dx.doi.org/10.1021/am201499r | ACS Appl. Mater. Interfaces 2012, 4, 424–430

In_2O_3 and IT2. In Figure 7b, it was indicated that the In_2O_3–TiO_2 heteroarchitectures exhibited much lower emission intensity than In_2O_3, indicating that the recombination of the photogenerated charge carrier was inhibited greatly in the In_2O_3–TiO_2 heteroarchitectures. Since the In_2O_3 (h^+) radicals has a redoxpotential of about 2.17 eV vs NHE, it could oxidize a suitable substrate (R), together with recovery of the original In_2O_3. The mechanism for the photocatalytic degradation of RB in our experiment was proposed as follows

$$In_2O_3 + h\nu \rightarrow In_2O_3(CBe^- + VBh^+)$$

$$In_2O_3(e^-) + TiO_2 \rightarrow In_2O_3 + TiO_2(e^-)$$

$$TiO_2(e^-) + O_2 \rightarrow TiO_2 + \bullet O_2^-$$

$$\bullet O_2^- + H_2O \rightarrow HO_2\bullet + OH^-$$

$$HO_2\bullet + H_2O \rightarrow H_2O_2 + OH\bullet$$

$$H_2O_2 \rightarrow 2OH\bullet$$

$$OH\bullet + RB \rightarrow \text{degraded or mineralized products}$$

$$In_2O_3(h^+) + RB \rightarrow \text{degraded or mineralized products}$$

Under visible light irradiation, photogenerated electrons in In_2O_3 moved freely to the TiO_2, meanwhile, the photogenerated holes were left in the valence band of In_2O_3.[48,49] Dissolved oxygen molecules react with the surface of the TiO_2 electrons (e^-) to yield superoxide radical anions, $\bullet O_2^-$, which on protonation generate the hydroperoxy, $HO_2\bullet$, radicals, producing hydroxyl radical OH•, which was a strong oxidizing agent to decompose the organic dye.[50,51]

CONCLUSIONS

In summary, In_2O_3–TiO_2 heteroarchitectures fabricated via the electrospinning and solvothermal methods possessed higher photocatalytic activities than the pure TiO_2 and In_2O_3 for the degradation of RB dye under visible light irradiation. Furthermore, the In_2O_3–TiO_2 heteroarchitectures nanofibers could be easily recycled without decrease of the photocatalytic activity due to their one-dimensional nanostructure property. And, it is expected that the In_2O_3–TiO_2 heteroarchitectures nanofibers with high photocatalytic activity will greatly promote their practical application to eliminate the organic pollutants from wastewater.

AUTHOR INFORMATION

Corresponding Author

*E-mail: clshao@nenu.edu.cn (C.S.); chenb608@nenu.edu.cn (B.C.). Tel.: 8643185098803.

ACKNOWLEDGMENTS

The present work is supported financially by the National Natural Science Foundation of China (50572014 and 50972027), and the Program for New Century Excellent Talents in University (NCET-05-0322).

REFERENCES

(1) Fujishima, A.; Honda, K. *Nature* **1972**, *238*, 37.
(2) Wang, C.; Shao, C.; Liu, Y.; Li, X. *Inorg. Chem.* **2009**, *48*, 1105.
(3) Ye, C.; Bando, Y.; Shen, G.; Golberg, D. *J. Phys. Chem. B* **2006**, *110*, 15146.
(4) Zhang, L.; Wang, W.; Yang, J.; Chen, Z.; Zhang, W.; Zhou, L.; Liu, S. *Appl. Catal., A* **2006**, *308*, 105.
(5) Li, L.; Chu, Y.; Liu, Y.; Dong, L. *J. Phys. Chem. C* **2007**, *111*, 2123.
(6) Smith, Y, R.; Kar, A.; Subramanian, V. R. *Ind. Eng. Chem. Res.* **2009**, *48*, 10268.
(7) Mu, J. B.; Shao, C. L.; Guo, Z. C.; Zhang, Z. Y.; Zhang, M. Y.; Zhang, P.; Chen, B; Liu, Y. C. *ACS Appl. Mater. Interfaces* **2011**, *3*, 590.
(8) Fujishima, A.; Rao, T. N.; Tryk, D. A. *J. Photochem. Photobiol. C* **2000**, *1*, 1.
(9) Kamat, P. V. *Chem. Rev.* **1993**, *93*, 267.
(10) Hoffmann, M. R.; Martin, S. T.; Choi, W.; Bahnemann, D. W. *Chem. Rev.* **1995**, *95*, 69.
(11) Zhang, M. Y.; Shao, C. L.; Guo, Z. C.; Zhang, Z. Y.; Mu, J. B.; Cao, T. P.; Liu, Y. C. *ACS Appl. Mater. Interfaces* **2011**, *3*, 369.
(12) Liu, Y.; Li, J.; Wang, M. J.; Li, Z. Y.; Liu, H. T.; He, P.; Yang, X. R.; Li, J. H. *Cryst. Growth Des.* **2005**, *5*, 1643.
(13) Wang, G.; Wang, Q.; Lu, W.; Li, J. H. *J. Phys. Chem. B* **2006**, *110*, 22029.
(14) Linsebigler, A.; Lu, G.; Yates, J. T. *Chem. Rev.* **1995**, *95*, 735.
(15) Anpo, M.; Takeuchi, M. *J. Catal.* **2003**, *216*, 505.
(16) Diebold, U. *Surf. Sci. Rep.* **2003**, *48*, 53.
(17) Arana, J.; Diaz, O. G.; Saracho, M. M.; Rodriguez, J. M. D.; Melian, J. A. H.; Pena, J. P. *Appl. Catal., B* **2001**, *32*, 49.
(18) Choi, W.; Termin, A.; Hoffmann, M. R. *J. Phys. Chem.* **1994**, *98*, 13669.
(19) Wang, J. W.; Mao, B. D.; Gole, J. L.; Burda, C. *Nanoscale* **2010**, *2*, 2257.
(20) In, S.; Orlov, A.; Berg, R.; Garcia, F.; Pedrosa-Jimenez, S.; Tikho, M. S.; Wright, D. S.; Lambert, R. M. *J. Am. Chem. Soc.* **2007**, *129*, 13790.
(21) Sakthivel, S.; Kisch, H. *Angew. Chem., Int. Ed.* **2003**, *42*, 4908.
(22) Valentin, C. D.; Pacchioni, G.; Selloni, A. *Chem. Mater.* **2005**, *17*, 6656.
(23) Asahi, R.; Morikawa, T.; Ohwaki, T.; Aoki, K.; Taga, Y. *Science* **2001**, *293*, 269.
(24) Zhang, L. W.; Fu, H. B.; Zhu, Y. F. *Adv. Funct. Mater.* **2008**, *18*, 2180.
(25) Zhong, J.; Chen, F.; Zhang, J. L. *J. Phys. Chem. C* **2010**, *114*, 933.
(26) Zhao, L.; Chen, X. F.; Wang, X. C.; Zhang, Y. J.; Wei, W.; Sun, Y. H.; Antonietti, M.; Titirici, M. M. *Adv. Mater.* **2010**, *22*, 3317.
(27) Lettmann, C.; Hildenbrand, Kisch. H.; Macyk, W.; Maier, W. F. *Appl. Catal., B* **2001**, *32*, 215.
(28) Mitoraj, D.; Kisch, H. *Angew. Chem., Int.Ed.* **2008**, *47*, 9975.
(29) Dong, F.; Guo, S.; Wang, H. Q.; Li, X. F.; Wu, Z. B. *J. Phys. Chem. C* **2011**, *115*, 13285.
(30) Asahi, R.; Morikawa, T.; Ohwaki, T.; Aoki, K.; Taga, Y. *Science* **2001**, *293*, 269.
(31) Quarto, F.; Sunseri, C.; Piazza, S.; Romano, M. *J. Phys. Chem. B* **1997**, *101*, 2519.
(32) Lv, J.; Kako, T.; Li, Z. S.; Zou, Z. G.; Ye, J. H. *J. Phys. Chem. C* **2010**, *114*, 6157.
(33) Wang, Z. Y.; Huang, B. B.; Dai, Y.; Qin, X. Y.; Zhang., X. Y.; Wang, P.; Liu, H. X.; Yu, J. X. *J. Phys. Chem. C* **2009**, *113*, 4612.
(34) Chang, W. K.; Rao, K. K.; Kuo, H, C.; Cai, J. F.; Wong, M. S. *Appl. Catal., A* **2007**, *321*, 1.
(35) Shchukin, D.; Poznyak, S.; Kulak, A.; Pichat, P. *J. Photochem. Photobiol. A* **2004**, *162*, 423.
(36) Poznyak, S. K.; Talapin, D. V.; Kulak, A. I. *J. Phys. Chem. B* **2001**, *105*, 4816.
(37) González, V. R.; Rodrǵuez, A. M.; May, M.; Tzompantzi, F.; Gómez, R. *J. Photochem. Photobiol., A* **2008**, *193*, 266.
(38) Poznyak, S. K.; Talapin, D. V.; Anatoly, I. K. *Thin Solid Films* **2002**, *405*, 35.
(39) Reddya, B. M.; Chowdhury, B.; Smirniotis, P. G. *Appl. Catal., A* **2001**, *219*, 53.
(40) Yang, X.; Wang, Y.; Xu, L.; Yu, X.; Guo, Y. *J. Phys. Chem. C* **2008**, *112*, 11481.
(41) Pujilaksono, B.; Klement, U.; Nyborg, L.; Jelvestam, U.; Hill, S.; Burgard, D. *Mater. Charact.* **2005**, *54*, 1.

(42) Zschoerper, N.; Katzenmaier, V.; Vohrer, U.; Haupt, M.; Oehr, C.; Hirth, T. *Carbon* **2009**, *47*, 2174.
(43) Gurlo, A.; Barsan, N.; Weimar, U.; Ivanovskaya, M.; Taurino, A.; Siciliano, P. *Chem. Mater.* **2003**, *15*, 4377.
(44) Li, J. H.; Shen, D. Z.; Zhang, J. Y.; Zhao, D. X.; Li, B. S.; Lu, Y. M.; Liu, Y. C.; Fan, X. W. *J. Magn. Magn. Mater.* **2006**, *302*, 118.
(45) Turchi, C.; Ollis, D. *J. Catal.* **1990**, *122*, 178.
(46) Lee, M.; Park, S.; Lee, G.; Ju, C.; Hong, S. *Catal. Today* **2005**, *101*, 283.
(47) He, T.; Ma, Y.; Cao., Y.; Hu, X.; Liu, H.; Zhang, G.; Yang, W.; Yao, J. *J. Phys. Chem. B* **2002**, *106*, 12670.
(48) Zhang, H.; Lv, X. J.; Li, Y. M.; Wang, Y.; Li, J. H. *ACS Nano* **2010**, *4*, 380.
(49) Li, J. H.; Zhang, J. Z. *Coord. Chem. Rev.* **2009**, *253*, 3015.
(50) Aarthi, T.; Madras, G. *Ind. Eng. Chem. Res.* **2007**, *46*, 7.
(51) Rajeshwar, K.; Osugi, M.; Chanmanee, W.; Chenthamarakshan, C.; Zanoni, M.; Kajitvichyanukul, P.; Krishnan, A. R. *Photochem. Photobiol. C* **2008**, *9*, 171.